



Effect of Co-doped graphene quantum dots to polyaniline ratio on performance of supercapacitor

Abdallah Ramadan¹ · M. Anas¹ · Shaker Ebrahim² · Moataz Soliman² · Aly Abou-Aly¹

Received: 2 December 2019 / Accepted: 21 March 2020 / Published online: 31 March 2020
© Springer Science+Business Media, LLC, part of Springer Nature 2020

Abstract

Sulfur and nitrogen co-doped graphene quantum dots (S,N:GQDs) were prepared by a hydrothermal method. A series of polyaniline/S,N:G QDs nanocomposites (PGQD_x where *x* is the mass of S,N:GQDs and equal to 0, 10, 20, 30, and 40 mg) has been synthesized via chemical in situ polymerization process. The UV–vis and Fourier transform infrared (FTIR) spectra showed an extra-doping level in H₂SO₄-doped polyaniline (PANI) due to –COOH groups of GQDs. However, increasing of GQDs content enhanced the aggregation of GQDs and reduced the doping level. The surface morphologies of nanocomposites showed a mixed of nanofibers, granules, and flakes with highly porous structure and particle size varied from 50 to 70 nm. Electrochemical properties of PGQD nanocomposites cast onto nickel-foam substrate as a supercapacitor electrode were performed in 2 M KOH electrolyte using cyclic voltammetry, charge/discharge, and electrochemical impedance techniques. PGQD20 exhibited maximum specific capacitance of 2524 F/g at 2 A/g with an excellent cyclic stability of 100% after 1000 cycle at scan rate of 50 mV/s. GQDs with unique properties reduces the charge transfer resistances, and promotes the contact between polyaniline and electrolyte and the electrochemical performance.

1 Introduction

Supercapacitors are more appealing than other electrochemical energy storage device, such as batteries and fuel cells because of their distinctive characteristics including light weight, very small volume, and long-life cycle. The supercapacitor electrode possesses high power density similar to traditional capacitors existed in most electronic devices due to their unique charge storage mechanism [1]. Polyaniline (PANI) has been studied as a supercapacitor electrode with high specific capacitance due to low production cost, easy synthesis, controllable conductivity and fast charge/discharge. However, PANI electrode suffers from low stability and undergoes degradation through the reduction and oxidation reaction. Moreover, the chemical and mechanical changes of PANI electrode including swelling, shrinkage, and cracks during charging and discharging process effects

on rate capability, cycle stability, and electrochemical performance [2].

To improve the electrochemical performance and developed the energy and power densities of the supercapacitor electrode, PANI with high specific capacitance based on the pseudocapacitive behavior hybrids with carbon structure materials having a high surface area with electrical double layer capacitance (EDLC) was fabricated [3]. GQDs have excellent electronic, mechanical and optical properties, amazing water solubility, and negligible toxicity and can be replaced graphene sheets in different applications, such as bioimaging [4], optoelectronic devices [5], solar cells [6], photocatalysis [7], sensors [8], and heavy metal ion detection [9].

GQDs have been involved in the fabrication of supercapacitor electrodes due to their large specific surface area and high pseudocapacitance originated from functional groups, edges, defects, and dopants [10]. The doping of GQDs with sulfur and nitrogen (S,N:GQDs) can successfully create more catalytically active sites [11], broad photoabsorption in wide-range spectra, high carrier transport mobility, and good chemical stability [12].

Ouyang et al. synthesized S,N:GQDs with high crystallinity by a top-down hydrothermal method and a low specific capacitance of 362.6 F/g at a scan rate 5 mV/s

✉ Abdallah Ramadan
abdallah_ramadan@alexu.edu.edu.eg

¹ Physics Department, Faculty of Science, Alexandria University, Moharram Bek, Alexandria 21511, Egypt

² Department of Materials Science, Institute of Graduate Studies and Research, Alexandria University, 163 Horrya Avenue, El-Shatby, Alexandria 21526, Egypt

was obtained [13]. Malik et al. [14] prepared GQDs by top-down route from graphene oxide flakes and followed by synthesis GQD-PANI by polymerization of aniline. The GQD-PANI composite showed a relatively high specific capacitance of 1044 F/g at 1 A/g with 80.1% retention of capacitance after 3000 cycle. Dinari et al. [15] prepared S,N:GQD-PANI composite by electropolymerization of aniline using titanium electrode and 0.5 M H₂SO₄ in the presence of S,N:GQDs by cyclic voltammetry, where the S,N:GQDs was synthesized using the hydrothermal method. Although Dinari et al. applied this composite as a supercapacitor electrode but they did not accomplish the electrochemical performance including specific capacitance, energy density values, and cyclic stability. Moreover, they used glassy carbon and titanium sheet as substrates.

The main objective of this work is to produce high performance and stable supercapacitor electrode with a specific capacitance of 2524 F/g at 2 A/g based on PANI/S,N:GQD nanocomposite and nickel-foam substrate. The effect of S,N:GQDs to polyaniline ratio on performance of supercapacitor electrode is investigated. PGQD nanocomposites with different S,N:GQD contents via in situ chemical polymerization are carried out. The electrochemical properties of PGQD nanocomposites cast onto nickel-foam substrate as a supercapacitor electrode are evaluated using cyclic voltammetry, charge/discharge, and electrochemical impedance techniques. The retentions capacitance for 1000 cycle is performed as indicators for the supercapacitor stability of PANI and PGQD nanocomposite electrode.

2 Experimental work

2.1 Materials

Aniline monomer, citric acid, and *N*-methyl-2-pyrrolidone (NMP, 98%) were obtained from Loba Chemie. Ammonium peroxodisulfate (APS) was purchased from Chem-Lab. Thiourea and KOH were obtained from local chemical companies. Sulfuric acid (95–97%), hydrochloric acid (30–34%), and polyvinylidene difluoride (PVDF) powder were obtained from J. T. Baker, SDFCL, and Alfa Aesar, respectively. Ethanol (99.8%) and dimethylformamide (DMF, 99%) were purchased from Fisher. All chemicals were used without further purification.

2.2 Synthesis of S,N:GQDs

S, N: GQDs were synthesized by hydrothermal method using citric acid as carbon source and thiourea as S, N source [16]. Typically, 15 mmol citric acid and 45 mmol

thiourea were dissolved in 75 mL deionized water to form a clear solution. After that this solution was transferred into a 300 mL Teflon-lined stainless autoclave and placed at 160 °C for 4 h. The final product was precipitated collected by adding 50 mL ethanol into the solution, and centrifuged at 10,000 rpm for 10 min. The obtained solid was easily dispersed into water.

2.3 Synthesis of PANI/S,N:GQDs

PANI/S,N:GQDs (PGQDs) nanocomposites were synthesized via chemical oxidation polymerization of PANI in situ GQDs as shown in Scheme 1. Typically, 10, 20, 30, and 40 mg of S,N:GQDs were dispersed in 20 mL deionized water using ultrasonication for 20 min and 200 µL aniline followed by 0.5 M H₂SO₄ was added and sonicated for another 30 min. After that 20 mL deionized water containing 0.5 g APS as an oxidant was added to the above mixture under stirring (molar ratio between aniline and APS is 1:1). The resulting mixture was allowed to stand for 5 h in the ice bath and the stirring was continued for overnight. The product was filtered and washed with deionized water and ethanol for several times to remove the excess of APS. Finally, the product was dried in vacuum oven at 60 °C overnight to get PGQDs nanocomposite by the interaction between –NH groups of PANI and carboxylic (–COO) groups of GQDs as shown in Scheme 1. Pure PANI without S,N:GQDs was prepared by the same method. The samples were denoted by PANI, PGQD10, PGQD20, PGQD30, and PGQD40 according to the content of GQDs.

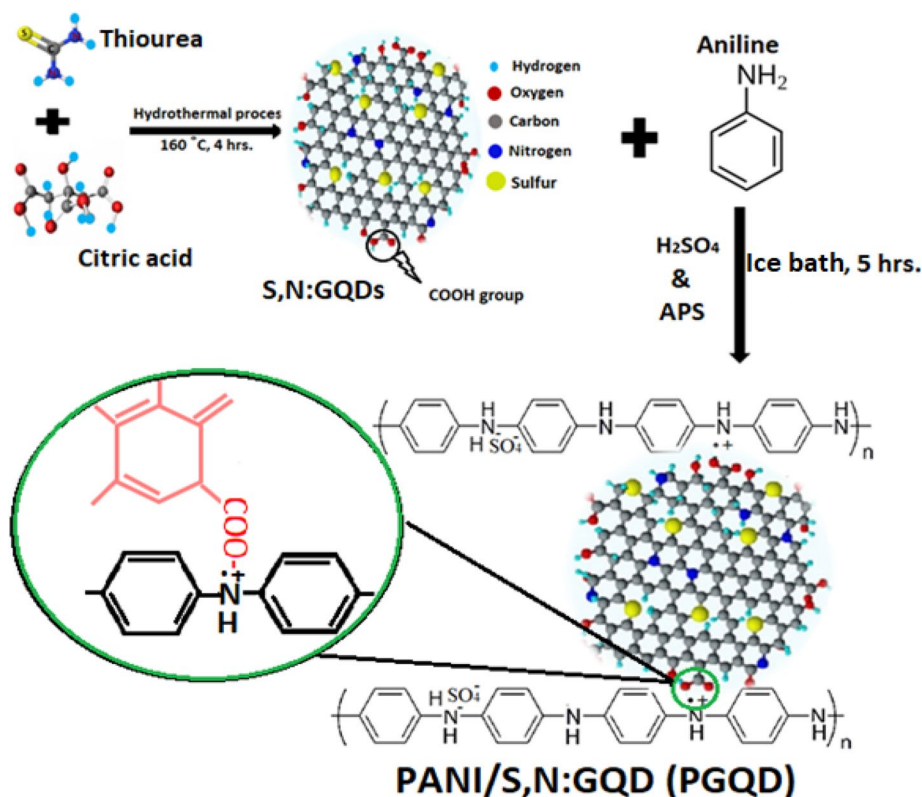
2.4 PGQD electrode preparation

Nickel foam (NF) (approximately 1 × 4.5 cm²) as a current collector was cleaned in 1 M HCl solution in the sonication bath for 20 min to remove the NiO layer formed onto the NF surface and then washed in an ultrasonic bath with deionized water and absolute ethanol. The working electrode was prepared by mixing 80% of PGQD as an active material, 10% carbon black, 10% PVDF, 0.3 mL of NMP, and followed by 0.3 mL of ethanol. This mixture was dropped onto the NF. The pressed loading mass on NF electrode was about 1.5 mg, and dried at 60 °C overnight.

2.5 Characterization techniques

The UV–VIS spectra of PGQDs nanocomposites dispersed in DMF by sonication were recorded in the range of 300 to 1100 nm using Thermo (Evolution 300). Photoluminescence (PL) measurements were executed by a (Perkin

Scheme 1: Synthesis steps of S,N:GQDs and PANI/S,N:GQDs (PGQD) nanocomposites



Elmer LS-55) spectrometer at room temperature. Fourier Transform Infrared FT-IR (PerkinElmer-Spectrum 2B, USA) spectrophotometer over a wavenumber in the range from 400 to 4000 cm^{-1} was used to identify the structures of PGQDs nanocomposites pressed with potassium bromide pellet. For characterizing the chemical bonding structure, Raman spectrometer (Senterra Bruker, Germany) was used at excitation wavelength of 532 nm. The structural characterization was carried out using X-ray diffractometer (XRD-7000 Shimadzu-Japan) with a Cu-K α radiation ($\lambda = 1.54060 \text{ \AA}$) operating at 40 kV and 30 mA with a scan rate of $10^\circ \text{ min}^{-1}$ over 2θ between 5° and 80° . Scanning electron microscopy (SEM) was performed using JSM-IT200 instrument operated at an acceleration voltage of 20 kV. Transmission electron microscopy (TEM) was executed using JEOL (JEM-2100 LaB6) Japan. Brunauer–Emmett Teller (BET) surface area test was performed using Belsorp Mini II (BEI Japan Inc., Ltd.), where the samples were degassed under vacuum at 160°C for 4 h before the measurement.

2.6 Electrochemical test

Electrochemical properties of the pure PANI, PGQD10, PGQD20, PGQD30, and PGQD40 nanocomposites were evaluated as electrode materials for supercapacitors using

cyclic voltammetry (CV), galvanostatic charge–discharge (GCD), and electrochemical impedance spectroscopy (EIS) with a three-electrode setup in 2 M KOH using OrigaFlex-OGF05 (Origalys, France). Cyclic voltammetry was performed for the prepared samples in the potential range from 0 to 0.6 V at scan rate ranging from 5 to 50 mV/s. The specific capacitance (C_s in F/g) was estimated from the area enclosed in cyclic voltammogram $\int_{v_i}^{v_f} I(V)dV$ using the following equation [17]:

$$C_s(\text{F/g}) = \frac{\int_{v_i}^{v_f} I(V)dV}{2sm\Delta V} \quad (1)$$

where m is the mass of the active material on the electrode (g), ΔV is a potential window (V), and s is the scan rate mV/s.

For GCD measurements, we applied a constant current on the supercapacitor electrode for charging and discharging and the C_s related to the discharge current (I) and the time of discharge (t) is given by the following relation [18, 19]:

For GCD measurements, we applied a constant current on the supercapacitor electrode for charging and discharging and the C_s related to the discharge current (I) and the time of discharge (t) is given by the following relation [18, 19]:

$$C_s(F/g) = \frac{It}{m\Delta V} \quad (2)$$

where ΔV is the working potential (V).

The energy density (E) and power density (P) can be calculated using the following equations [20, 21]:

$$E(W\ h/Kg) = \frac{1}{2} * C_s * V^2 * \frac{1000}{3600} \quad (3)$$

$$P(W/Kg) = \frac{E}{t} * 3600 \quad (4)$$

3 Results and discussion

3.1 Absorption property

The absorption spectrum of S,N:GQDs presented in Fig. 1a shows three absorption peaks at 245, 332, and 590 nm. The first two peaks belong to the GQDs and are due to $\pi \rightarrow \pi^*$ of C=C and $n \rightarrow \pi^*$ transition of the C=O bond, respectively and these spectra are similar to the GQDs prepared by a chemical cutting of oxidized graphene sheets [22]. The third peak at 590 nm confirms the doping process with sulfur and may be attributed to $n \rightarrow \pi^*$ of S=O [16].

The PL spectra of S,N:GQDs solution with different excitation wavelengths from 320 to 500 nm is shown in Fig. 1b. The S,N:GQDs exhibit excitation independent PL spectra of emission peak at 442 nm with excitation in the region from 320 to 380 nm. The PL intensity of S,N:GQDs is increased with rising the excitation wavelength from 320 to 340 nm. The PL intensity is steadily decreased with further increase in the excitation wavelength after 340 nm. The excitation-independent PL spectra is attributed to the high uniformity in the size of sp^2 clusters of S,N:GQDs [16, 23, 24]. When the excitation wavelength exceeds 380 nm, weak PL emission spectra with an excitation dependent are observed in the inset of Fig. 1b. The position of PL spectra peaks is red shifted from 442 to 534 nm due to the existence of sulfur doping [16]. The functional groups, such as oxygen and nitrogen or S=O create energy levels and result in a series of emissive traps [13, 23].

Figure 1c displays the UV–visible spectra of pure PANI and PGQDs nanocomposite with different GQDs contents. For the spectra of pure PANI, three absorption bands at 356 nm, 435 nm, and 875 nm are attributed to the $\pi \rightarrow \pi^*$ transition of the benzenoid rings, polaron $\rightarrow \pi^*$, and $\pi \rightarrow$ polaron transitions, respectively [25]. In addition, the peaks at 435 and 875 nm are associated with the doping level and polaron band formation.

The absorption spectra of PGQDs are similar to the spectrum of pure PANI with a slightly shift of the absorption

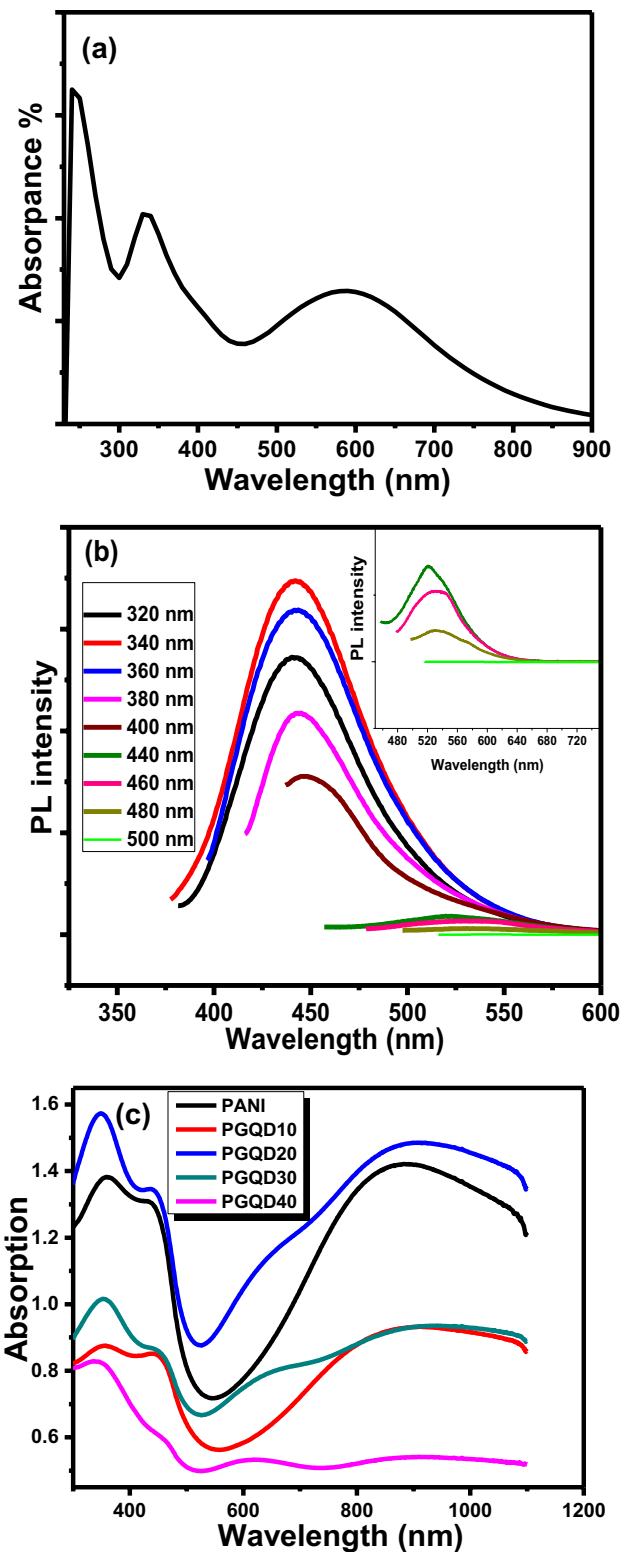


Fig. 1 a UV–vis spectrum S,N:GQDs, b PL spectra of S,N:GQDs at different excitation wavelengths, and c UV–vis spectra of PANI and different PGQD nanocomposites

Table 1 The assignments of UV–vis absorption peaks of pure PANI and PGQDs nanocomposites

Polymer	Wavelength of the absorption peaks			Absorption at ~ 875/ Absorption at ~ 350
	$\pi \rightarrow \pi^*$ transition	Polaron $\rightarrow \pi^*$ transition	$\pi \rightarrow$ polaron transition	
Pure PANI	358 nm	432 nm	875 nm	1.03
PGQD10	355 nm	440 nm	910 nm	1.066
PGQD20	350 nm	436 nm	908 nm	0.95
PGQD30	353 nm	446 nm	914 nm	0.92
PGQD40	344 nm	–	909 nm	0.65

peaks as reported in Table 1. The decrease in the absorption peak at 432 nm with increasing the S,N:GQDs content is observed and there is a new small peak appeared at 620 nm due to the dedoping of PANI chains [26]. Based on the previous research, the ratio between the intensities of absorption peaks at ~ 875 nm and at ~ 350 nm indicates the extent of doping level of PANI [27–29]. It is noticed that this ratio is the smallest for PGQD 40 and this accompany by the appearance of the peak at 620 nm of the emeraldine base.

3.2 Structural property

The FTIR spectrum is recorded in Fig. 2a to identify chemical functional groups of GQDs. The IR spectrum of S,N:GQDs shows a very broad absorption band centered at 3173 cm^{-1} and is assigned to stretching vibrations of O–H, N–H, and this is recognized the presence of amino and hydroxyl groups on the surface of GQDs. The characteristic band of graphite structure at 1582 cm^{-1} corresponds to the bending vibrations of C=C. The peak at 1400 cm^{-1} is assigned to the stretching vibration of C–N which validates the successful doping with N element. C=S stretching group appears in a wide region from 1000 to 1400 cm^{-1} while C–S stretching is observed at 617 cm^{-1} [16, 30].

In the FTIR spectrum of pure PANI shown in Fig. 2b, the main characteristic peaks of PANI are observed. The peaks at 1562 and 1476 cm^{-1} are corresponded to the stretching vibration modes C=C of the quinone diimine and benzenoid diamine units, respectively. In addition, the peaks at 1299 and 1105 cm^{-1} are due to C–N stretching of the secondary aromatic amine and the polaron band vibration peak associated with doping, respectively [31]. The peak appearing at 795 cm^{-1} is attributed to an aromatic C–H out-of-plane bending vibration. The presence of C–S group is confirmed by the appearance of peaks at about 616 cm^{-1} .

For PGQD nanocomposites, the spectra are similar to that of pure PANI, but the main characteristic bands have slightly shifted. The polaron band appeared at 1105 cm^{-1} of doped PANI shifts to higher energy at 1118 cm^{-1} in PGQD10 and this is attributed to an extra degree of doping [32]. However, it is noted that this peak shifts to a lower energy with increasing of the GQDs content due to the self-aggregation

of GQDs. The intensity ratio between quinoid and benzenoid ring vibrational modes (I_Q/I_B) provides information on the degree of oxidation of the PANI [33, 34]. The values of relative intensity of I_Q/I_B are 1.01, 1.036, 1.002, 1.014, and 1.13 corresponding to pure PANI, PGQD10, PGQD20, PGQD30, and PGQD40, respectively. The relative intensities are close to unity indicating that PANI in PGQDs samples has an emeraldine form. PGQD40 has a high I_Q/I_B ratio, i.e. more oxidation of benzenoid rings to quinoid rings and more dedoping to PANI chains as expected from the absorption spectra. Moreover, the relative intensity of I_Q/I_B for PGQD20 is unity. This indicates that PGQD20 has a perfect emeraldine structure [34]. These results conform a strong interaction between PANI and S,N:GQDs.

Raman spectrum of S,N:GQDs presents two peaks at 1353 and 1568 cm^{-1} and a broad peak around 2800 cm^{-1} assigned to D, G, and 2D bands, respectively as shown in Fig. 2c. The position and the broadening of two-dimensional (2D) band characterize the multilayer of graphene sheets [35]. The D band or a disordered band in carbon nanostructures is related to the presence of sp^3 defects. The G band is also known a crystalline band or graphite band and is related to the in-plane vibration of sp^2 carbon. The relative intensity of D and G band (I_D/I_G) expresses the atomic ratio of sp^3/sp^2 and represents the degree of disorder. The I_D/I_G ratio of N,S:GQDs (0.85) is larger than that reported previously [16, 36]. However, it is lower than that of the original graphene film (~ 1.05) [37]. This result shows that S,N:GQDs are highly crystalline and graphitic structure.

After polymerization of aniline in situ S,N:GQDs, the Raman spectrum of PGQD20 exhibits a shift in the positions of D and G bands to higher frequency from 1353 to 1374 cm^{-1} and from 1568 to 1580 , respectively. This shift is attributed to the interaction between GQDs and PANI chains. However, the 2D band is disappeared, and this means that the Raman spectra cannot detect the multilayer of GQDs [38]. Such interaction can offer strong interfacial adhesion between PANI and GQDs and facilitates the electron transportation during redox reaction [39].

Figure 3 shows the XRD patterns of the S,N:GQDs, pure PANI, and PGQD nanocomposites. The pattern of S,N:GQDs exhibits two diffraction peaks at $2\theta = 11.6^\circ$ and

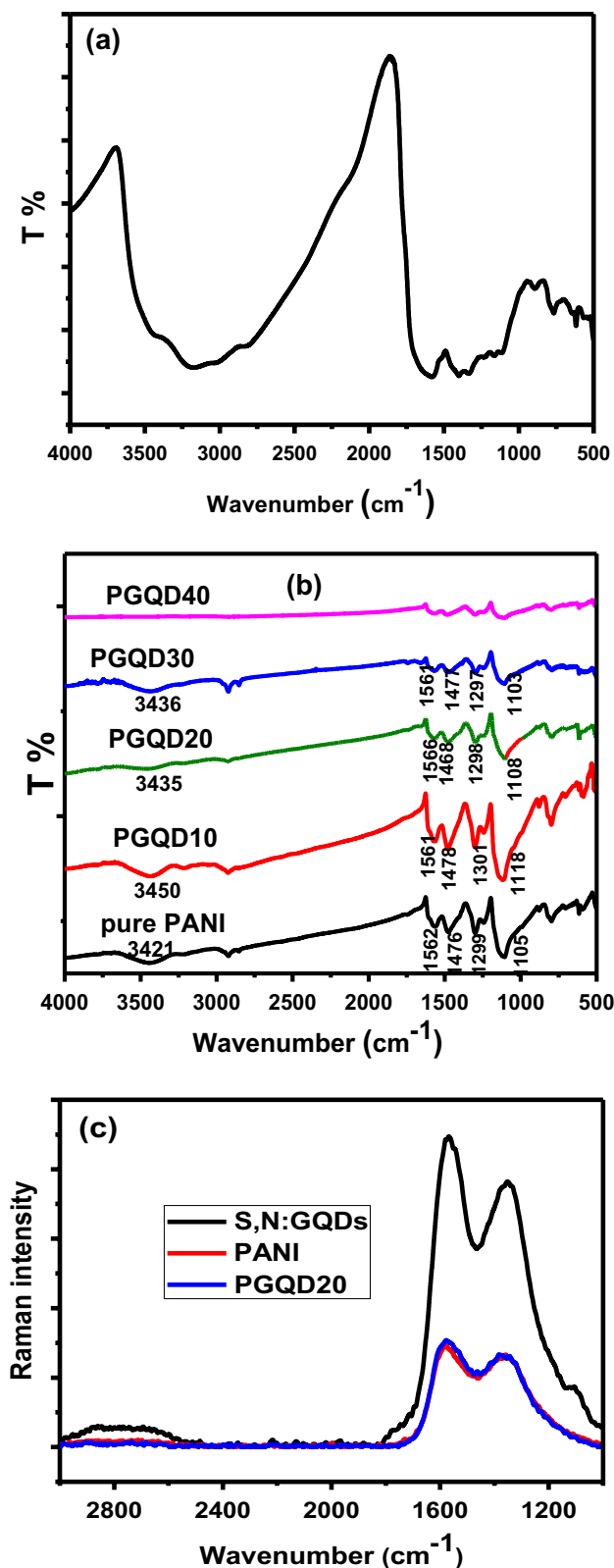


Fig. 2 FTIR spectra of a S,N:GQDs, b PANI, and PGQD nanocomposites, and c Raman spectra of S,N:GQDs, PANI, and PGQD20

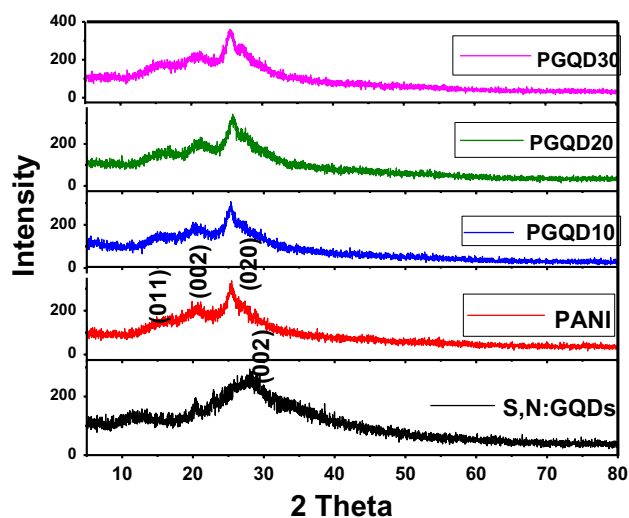


Fig. 3 XRD patterns of S,N:GQDs, PANI, and PGQD nanocomposites

28.16°. The broad peak at 28.16° is attributed to the inter-layer d-spacing of 3.16 Å according to Bragg's law and corresponds to the (002) plane of graphite structure. This value of d-spacing is less than the interlayer of graphite (3.35 Å) due to the effective π - π stacking of tiny graphene with few structural defects. For pure PANI, three diffraction peaks appeared at 15.9°, 20.3°, and 25.35° correspond to (011), (020), and (200) crystal planes of PANI and ascribe to parallel repeat units of PANI, periodicity parallel, and perpendicular to polymer chains, respectively [15, 40]. When S,N:GQDs are incorporated into the PANI matrix, the peak around 16° shifts to a lower angle and the broad peak of GQDs at 28.16° overlaps with the peak of PANI, and the results in a new peak in the composite at around 27°. The average crystallite sizes of the prepared nanocomposites calculated from XRD pattern using Scherrer's formula are 1.1, 4.2, 5.1, 4.9, and 5 nm for S,N:GQDs, PANI, PGQD10, PGQD20, and PGQD30, respectively.

3.3 Morphological study

The morphology of as-synthesized S,N:GQDs examined by TEM displays a good dispersion of GQDs without agglomeration with a size of 3–7 nm as shown in Fig. 4a. The high resolution TEM image (inset of Fig. 4a) elucidates the lattice spacing distance of 0.21 nm, which is close to the (100) facet of graphite [41]. The surface morphologies of pure PANI and PGQD nanocomposites are investigated as shown in Fig. 4b. Mixed of nanofibers, granules, and flakes with highly porous structure is clearly visible in pure PANI. The nanofibers morphology of PANI is related to the fast mixing of monomer and oxidant during polymerization in the initial stage [42, 43]. The fast consumption of oxidant can easily

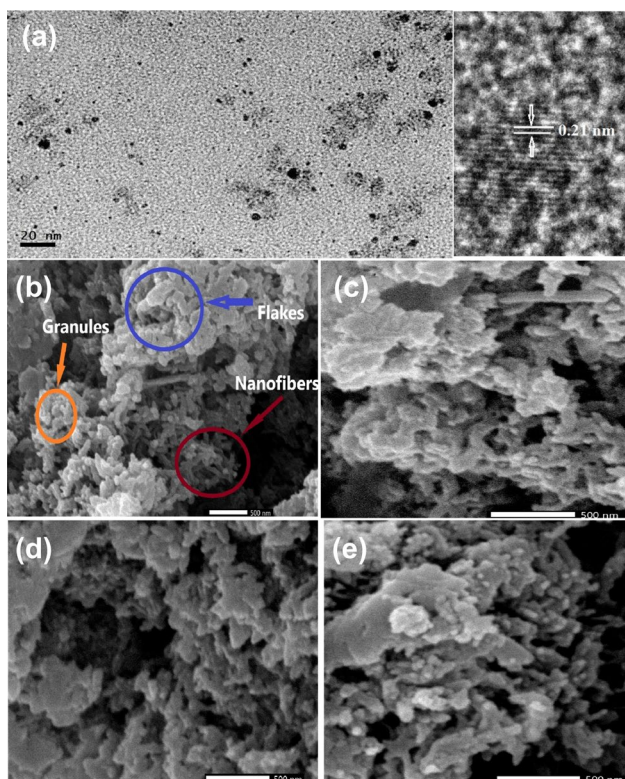


Fig. 4 a TEM image of S,N:GQDs and high-resolution TEM image is inserted as inset, SEM images of b pure PANI, c PGQD10, d PGQD20, and e PGQD30 nanocomposites

produce 1D nanostructure (nanofibers) and avoids overgrowth of PANI by additional polymerization [44]. The size of PANI nanoparticles measured from SEM image is varied from 50 to 70 nm which is very larger than the size determined by XRD and this indicates that the PANI is a cluster of some crystallites. It is observed that the SEM image of PGQD10 nanocomposite is similar to that of pure PANI as shown in Fig. 3c. By increasing the GQDs content, the SEM images of PGQD nanocomposites (Fig. 4d and e) display a change of the nanofibers to granules due to aggregation of GQDs. Different morphologies with nanofibers network contribute to a high specific capacity by increases the specific surface area and reduce the diffusion resistance of the electrolyte ions into the matrix of the electrode.

3.4 Surface analysis

Pure PANI and PGQD nanocomposites are characterized by nitrogen adsorption/desorption tests at 77.0 K to investigate the specific surface area and pore size distribution and the isotherm plot of PGQD20 is given in Fig. 5. According to the IUPAC classification, all isotherm curves of the prepared nanocomposites correspond to type III with a hysteresis loop of type H3 [45]. The pore size distribution curves

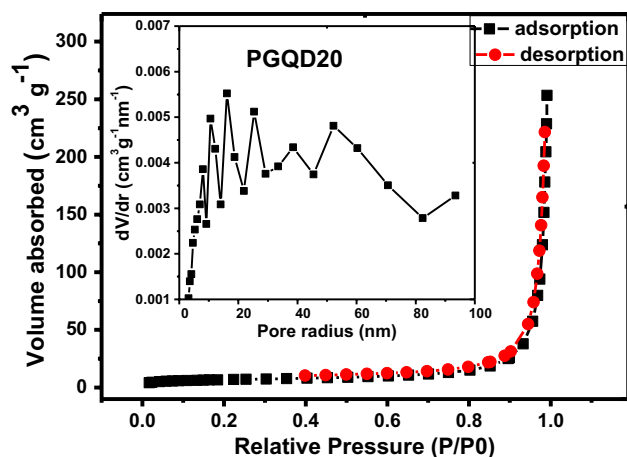


Fig. 5 Nitrogen adsorption/desorption and pore-size distribution isotherms are inserted as inset for PGQD20

according to Barrett–Joyner–Halenda (BJH) method in the inset of Fig. 5 show good distribution of pores in the range between 1 and 90 nm which indicates the meso/macroporous pores of adsorbent and few micropores in the nanocomposites. The BET specific surface area values are 30.8, 21.9, 24.06, and 28.9 m^2g^{-1} for pure PANI, PGQD10, PGQD20, and PGQD30, respectively. Based on BJH method, the total pore volumes of PANI, PGQD10, PGQD20, and PGQD30 at a relative pressure of 0.99 are 0.24, 0.28, 0.35, and 0.46 cm^3g^{-1} , respectively. It is found that the average pore diameters of PANI, PGQD10, PGQD20, and PGQD30 are 31.7, 51.9, 58.7, and 63 nm, respectively. This increase in average pore diameter is associated with microporous blockage or enhancement the size of macroporous of the nanocomposites. As the increase in S,N:GQDs content, the specific surface area of PGQD10 is found to be less than the specific surface area of pure PANI. This behavior is due to intercalated of S,N:GQDs into PANI matrix and the disappearance of micropores during the polymerization process. In other words, the small content of S,N:GQDs enhances the doping level of PANI and reduces its specific surface area. The BET surface area values of PGQD20 and PGQD30 are increased and this is related to the high value of the free volume of PANI [46]. The existence meso/macroporous structure of the PGQDs nanocomposites provides the possibility of electrons and ions transportation, which lead to the high electrochemical performance of PGQDs nanocomposite electrodes.

3.5 Electrochemical analysis

CVs response of pure PANI, PGQD10, PGQD20, PGQD30, and PGQD40 cast on NF substrate have been studied in 2 M KOH. Before performing the electrochemical experiments, the PGQDs electrodes are charged and discharged for 100

repetitive CV at a scan rate of 50 mV/s to achieve the stability in electrochemical performance. Initially, the PGQDs electrodes display some variations in their performance due to the insufficient wetting of the electrode surface by the electrolyte.

After about 100 cycle, the PGQDs electrodes exhibit steady electrochemical performance with a slight variation [47].

Figure 6a compares the cyclic voltammograms of different samples at scan rate of 5 mV/s in a voltage window from 0 to

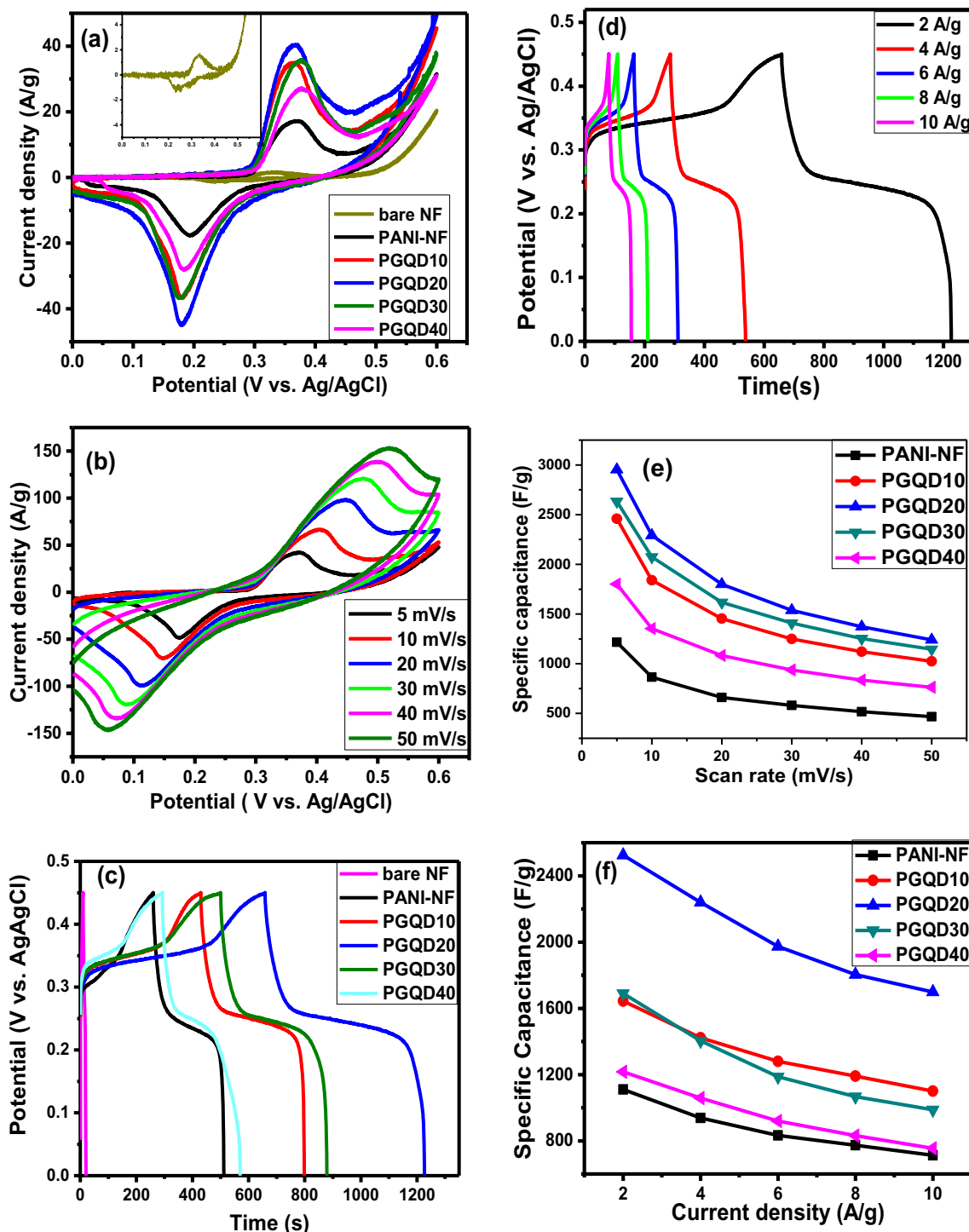


Fig. 6 a Cyclic voltammetry of bare NF, PANI-NF, and PGQD nanocomposites at scan rate 5 mV/s, inset is CV of bare NF, b Cyclic voltammetry of PGQD20 at different scan rate from 5 to 50 mV/s, c GCD behavior of PANI-NF and PGQD nanocomposites at current

density 2 A/g, d GCD curve of PGQD20 at different current density from 2 to 10 A/g, e The specific capacitance as a function of scan rate for PGQD nanocomposites and f the specific capacitance vs. the current density for PGQD nanocomposites

0.6 V. It is well known that PANI electrode is an inactive in neutral or alkaline solution. However, the CV curve of PANI-NF electrode exhibits a pseudocapacitance behavior with a pair of redox peaks (0.365/0.195 V) in alkaline electrolyte and this result is in agreement with the reported in the literatures [48–51]. This is attributed to the combined contributions from both NF and PANI. It is found that the CV of pure bare NF shows small redox peaks (0.334/0.246 V) with very small integrated area and specific capacitance of 83 F/g (assumed the loading mass is 1.5 mg) as depicted in the inset of Fig. 6a. The NF substrate plays a key role in providing high specific capacitance due to its redox reactions. On the other hand, the contribution of PANI results from the penetration and passivation of NF pores by PANI and this boosts the mass transfer process to enhance the redox reactions of Ni [51].

It is observed that PGQDs nanocomposites have higher integral area and specific capacitance than pure PANI. GQDs with unique properties reduces the charge transfer resistance and rises the contact between PANI and electrolyte and thus could improve the electrochemical performance [39]. The specific capacitances of 1216, 2458, 2953, 2633, and 1802 F/g correspond to PANI-NF, PGD10, PGQD20, PGQD30, and PGQD40, respectively. CV curves of PGQD20 display higher specific capacitance than other samples as shown in Fig. 6a. The different in the position of redox peaks can be ascribed to the variation in the polarization of the electrodes during CV test. The superior electroactivity of PGQD nanocomposites in alkaline solution is resulted from the strong interface interaction through the π - π stacking. In addition, the hydrogen bonding between PANI and S,N:GQDs facilitates the electron delocalization and dope PANI mainly by charge transfer occurred in redox process [52].

To examine the influence of scan rate on electrochemical performance, Fig. 6b shows the CVs of PGQD20 at different scan rates from 5 to 50 mV/s. The area under the CV curves increases. It is noted that the shape of the oxidation/reduction peaks at different scan rates is the same indicating the excellent rate capability and electrochemical reversibility of the nanocomposite electrode. In addition, the oxidation/reduction peaks are shifted to the positive/negative directions with increasing the scan rates due to the change of the internal resistance of the electrode materials [53]. The specific capacitance values of PGQD20 based on CV measurements are calculated to be 2953, 2291, 1800, 1538, 1372, and 1240 F/g at scan rate of 5, 10, 20, 30, 40, and 50 mV/s, respectively. At low scan rate, the electrolyte ions can diffuse and migrate into active material and consequently high specific capacitances are produced. On the other hand, the lower specific capacitances of supercapacitor electrode at high scan rate are attributed to inaccessibility of electrolyte ions to some active surface sites [54, 55].

The electrochemical performance parameters of PGQDs nanocomposites are further calculated using GCD analysis

at the current density ranging from 2 to 10 A/g. Figure 6c depicts the GCD for the prepared electrodes at 2 A/g between 0.0 and 0.45 V. The deviation from the linearity observed in charge and discharge curves confirms the pseudocapacitive behavior. The specific capacitance values based on GCD measurements for PANI-NF, PGQD10, PGQD20, PGQD30, and PGQD40 are found to be 1110, 1644, 2524, 1690, and 1217 F/g, respectively. These values agree with the specific capacitance values calculated by the cyclic voltammogram.

The value of specific capacitance of blank NF substrate is 40 F/g at a current density of 3 mA/cm². This means that the contribution of blank NF in specific capacitance is negligible when compared with the PGQDs active materials. However, NF plays as a good current collector and provides tracks for electrons/ions transport [47].

The charge/discharge curves of the PGQD20 electrode at different current densities of 2–10 A/g have the same shape as shown in Fig. 6d. Also, the specific capacitance values of PGQD20 are 2524, 2240, 1973, 1804, 1699 F/g at 2, 4, 6, 8, and 10 A/g, respectively. These results indicate sustainable performance of PGQD20 electrode in a wide current range [3]. The decrease in specific capacitance at elevating current density reflects that the decline in electrochemical performance at high current densities is due to the inaccessibility of electroactive sites by the electrolyte ions.

The specific capacitance values of PANI-NF and PGQD-NF nanocomposites calculated based on CV measurements as a function of scan rate are plotted in Fig. 6e. It is observed that the specific capacity of PANI and PGQDs nanocomposites gradually decreases with an increase in the scan rate from 5 to 50 mV/s. The fall in specific capacitance is due to decreasing of electron/ion diffusion at higher scan rate [41, 56]. In addition, the relation of the specific capacitance as a function of the discharge current density of PANI and PGQD nanocomposites is plotted in Fig. 6f. The capacitance retention rates of PANI, PGQD10, PGQD20, PGQD30, and PGQD40 are 64%, 67%, 67.5%, 59%, and 62% at 10 A/g, respectively. The best capability rate of PGQD20 is achieved.

Figure 7a demonstrates the Ragone plots of the PGQDs nanocomposites electrodes, where the specific energy and specific power were computed based on Eqs. (3) and (4), respectively. The energy densities at 2 A/g are 31.2, 46.2, 71, 47.5, and 34.2 Wh/kg for PANI, PGQD10, PGQD20, PGQD30, and PGQD40, respectively. PGQD20 displays a broad range of power density while it retains a relatively high energy density. At a power density of 450 W/kg, the PGQ20 electrode exhibits an energy density value of 71 Wh/kg, whilst the delivered energy density can remain 47.78 Wh/kg at a high-power density of 2250 W/kg.

To gain further insights about the excellent electrochemical performance of PGQDs nanocomposites, EIS is conducted at the open circuit voltage (OCV) in a frequency

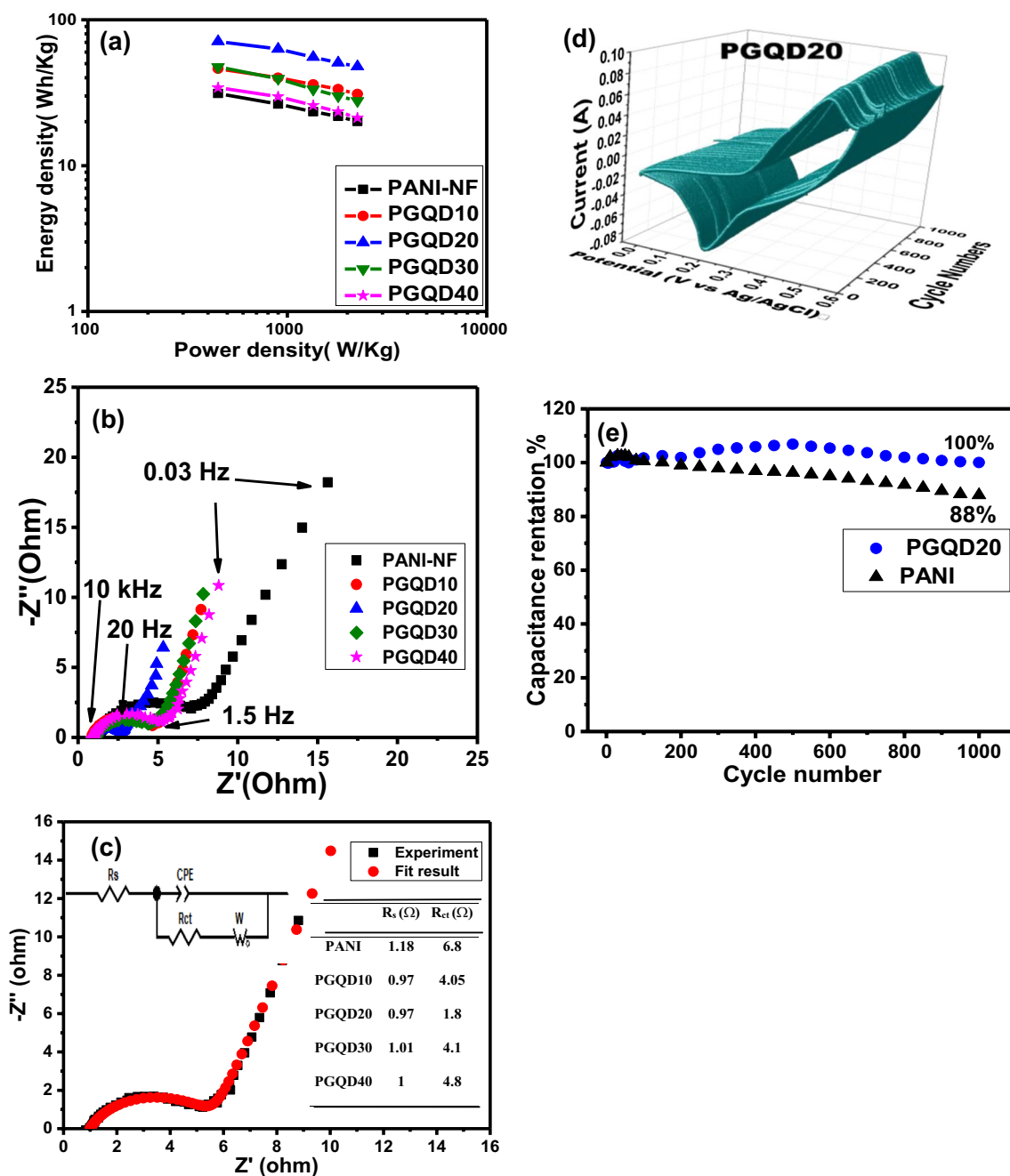


Fig. 7 **a** Ragone plots of supercapacitor electrodes based on PANI-NF and PGQD nanocomposites, **b** Nyquist plots of PGQD supercapacitor electrodes in 2 M KOH electrolyte, **c** Nyquist plots of experimental impedance data and fitting results for the PGQD40 electrode, inset is the electrical equivalent circuit and the fitted values of R_s and R_{ct} . (Z' real part of impedance, Z'' imaginary part of impedance, R_s

range from 10 kHz to 0.03 Hz. Figure 7b shows EIS in the form of the Nyquist plots for PANI and PGQDs nanocomposites. EIS spectra are fitted by the electrical equivalent circuit using ZView software provided in Fig. 7c. The fitting parameters of equivalent series resistance (R_s) and charge transfer resistance (R_{ct}) in the electrical equivalent circuit

series resistance, R_{ct} charge transfer resistance, W Warburg impedance, CPE constant phase element, **d** 3D-CV curves of the PGQD20 electrode measured at scan 50 mV/s, and **e** cyclic performance of pure PANI and PGQD20 supercapacitor electrodes at the scan rate of 50 mV/s

are listed in the inset of Fig. 7c. The EIS spectra of PANI and PGQDs nanocomposites exhibit a clear semi-circle in the middle-frequency domain and a nearly straight line sloped by 45° in the low-frequency domain, indicative of low R_{ct} and Warburg element (W). Besides, the intercept at Z' -axis denotes to R_s . EIS studies present that PGQDs

Table 2 Electrochemical performance of different supercapacitor electrode materials based on GQDs or PANI reported in previous works

Active material	Electrolyte	Substrate	Specific capacitance	Capacitance retention	Ref
S,N:GQDs	2 M KOH	Glassy carbon	362.6 F/g at 5 mV/s	–	[13]
GQD/PANI	0.5 M H ₂ SO ₄	Glassy carbon	1044 F/g at 1 A/g	80.1% after 3000 charge/discharge cycles	[14]
CQDs/PANI	1 M H ₂ SO ₄	Carbon fiber	738.3 F/g at 1 A/g	78% after 1000 charge/discharge cycles	[39]
N-CQDs/PANI	1 M H ₂ SO ₄	Carbon plate	498.3 F/g at 1 A/g	36.2% after 2000 charge/discharge cycles	[61]
PANI-S,N:GQDs @CeO ₂	1 M H ₂ SO ₄	Carbon fiber	270 F/g at 1 A/g	75% after 1000 charge/discharge cycles	[62]
Graphene/MnO ₂ /PANI	6 M KOH	Nickel foam	1081 F/g at 1 mV/s	99% after 1000 charge/discharge cycles	[63]
PGO@PANI	6 M KOH	Nickel foam	603 F/g at 1 A/g	77% after 1500 charge/discharge cycles	[17]
NiMoO ₄ -PANI	6 M KOH	Nickel foam	1214 F/g at 1 A/g	80.7% after 2000 charge/discharge cycles	[59]
GO/PANI/Ni(OH) ₂	6 M KOH	Nickel foam	743 F/g at 1 mV/s	84.4% after 2000 charge/discharge cycles	[64]
GQDs/NiCo-LDH	2 M KOH	Nickel foam	2220 F/g at 1 A/g	75.3% after 5000 charge/discharge cycles	[65]
CQDs/Co ₃ O ₄	2 M KOH	Nickel foam	1603 F/g at 1 A/g	97% after 2000 charge/discharge cycles	[66]
MnCo ₂ O _{4,5} /GQD	2 M KOH	Nickel foam	1625 F/g at 1 A/g	80% after 5000 charge/discharge cycles	[21]
GQD/CuCo ₂ S ₄	3 M KOH	Nickel foam	1725 F/g at 0.5 A/g	90% after 10,000 charge/discharge cycles	[67]
PANI/S, N:GQDs	2 M KOH	Nickel foam	2524 F/g at 2 A/g	100% after 1000 CV cycles	This work

nanocomposites electrodes with different N,S:GQDs contents have small R_s and consequently small internal resistances of the entire electrodes compared with the pure PANI electrode are expected. The values of R_{ct} extracted from the diameter of semicircle consistent with the capacitive performance of the prepared electrodes [57]. The R_{ct} of pure PANI (6.8 Ω) illustrates larger value compared with PGQDs nanocomposites. This can be explained based on the GQDs have a crucial role in decreasing the electrochemical impedance of the electrode materials and hence increase the capacitive performance. The R_{ct} value of the PGQD20 electrode (1.8 Ω) is also clearly smaller than other electrodes suggesting that it has a better electron transport [58]. Briefly, the PGQD20 electrode displays small R_s and R_{ct} indicating a better capacitive behavior [59].

3D cycling stability test of PGQD20 electrode was carried out in 2 M KOH electrolyte based on repeating the CV test between 0 and 0.6 V (vs. Ag/AgCl) at scan rate of 50 mV/s for 1000 cycle as shown in Fig. 7d. 3D plots can clearly illustrate the change in CVs over the number of cycles and, in this case, the plots show that the CVs preserve their original shapes after 1000 cycles [56, 60]. Figure 7e displays the specific capacitance retention for PGQD20 and pure PANI electrodes as a function of cycle number. The PGQD20 electrode shows exceptional cycling stability with 100% capacitance retention after 1000 cycle. However, due to swelling/shrinkage of PANI during redox reactions, pure PANI electrode exhibits 88% capacitance retention after 1000 cycle. It is noticed that after 500 cycle, the specific capacitance of PGQD20 electrode increases by 6.8% to reach the stability state. After that, the specific capacitance is slowly decreased. The improvement in cycle stability for PGQD20 is attributed to the synergistic effect of PANI and S,N:GQDs where the addition of S,N:GQDs to PANI

reduces the mechanical deformation of PANI chains during the repetitive redox reaction. This result reveals that the PGQD20 electrode appears good cycle stability and it has a great potential in supercapacitor application. The electrochemical performance of PGQDs nanocomposites electrodes is compared with others supercapacitor electrodes published in the literatures as shown in Table 2.

4 Conclusion

PGQDs nanocomposites were prepared via in situ chemical polymerization process. The morphological results showed that 3–7 nm GQDs are homogeneously distributed on the surface of PANI nanofibers. FTIR spectra of PGQD20 showed partially oxidized emeraldine form with unity of relative intensity of I_Q/I_B . The specific capacitance values of pure PANI of 1080 F/g at current density 2–10 A/g were obtained. PGQD20 nanocomposite presented superior specific capacitances of 2524–1699 F/g at 2–10 A/g and the energy density of PGQD20 was 71 W h/kg at 2 A/g with exceptional cyclic stability of 100% under 1000 cycle. The incorporation of GQDs into PANI matrix enhanced the capacitive performance of PGQD20 nanocomposite by providing the electrochemical active sites, reducing the charge transfer resistance and increasing the ion diffusion capability.

References

1. H. Gómez, M.K. Ram, F. Alvi, P. Villalba, E. Stefanakos, A. Kumar, J. Power Sources **196**, 4102 (2011). <https://doi.org/10.1016/j.jpowsour.2010.11.002>
2. J. Luo, W. Zhong, Y. Zou, C. Xiong, W. Yang, J. Power Sources **319**, 73 (2016). <https://doi.org/10.1016/j.jpowsour.2016.04.004>

3. H.-P. Cong, X.-C. Ren, P. Wang, S.-H. Yu, *Energy Environ. Sci.* **6**, 1185 (2013). <https://doi.org/10.1039/C2EE24203F>
4. S. Zhu, J. Zhang, C. Qiao et al., *Chem. Commun.* **47**, 6858 (2011). <https://doi.org/10.1039/C1CC11122A>
5. X. Li, M. Rui, J. Song, Z. Shen, H. Zeng, *Adv. Funct. Mater.* **25**, 4929 (2015). <https://doi.org/10.1002/adfm.201501250>
6. L. Chen, C.X. Guo, Q. Zhang et al., *ACS Appl. Mater. Interfaces.* **5**, 2047 (2013). <https://doi.org/10.1021/am302938a>
7. Z. Ma, H. Ming, H. Huang, Y. Liu, Z. Kang, *New J. Chem.* **36**, 861 (2012). <https://doi.org/10.1039/C2NJ20942J>
8. J. Shen, Y. Zhu, X. Yang, C. Li, *Chem. Commun.* **48**, 3686 (2012). <https://doi.org/10.1039/C2CC00110A>
9. S.L. Ting, S.J. Ee, A. Ananthanarayanan, K.C. Leong, P. Chen, *Electrochim. Acta* **172**, 7 (2015). <https://doi.org/10.1016/j.electacta.2015.01.026>
10. Y. Yan, J. Gong, J. Chen et al., *Adv. Mater.* **31**, 1808283 (2019). <https://doi.org/10.1002/adma.201808283>
11. T. Fan, G. Zhang, L. Jian et al., *J. Alloy. Compd.* **792**, 844 (2019). <https://doi.org/10.1016/j.jallcom.2019.04.097>
12. H. Xie, C. Hou, H. Wang, Q. Zhang, Y. Li, *Nanoscale Res. Lett.* **12**, 400 (2017). <https://doi.org/10.1186/s11671-017-2101-1>
13. Z. Ouyang, Y. Lei, Y. Chen et al., *Nanoscale Res. Lett.* **14**, 219 (2019). <https://doi.org/10.1186/s11671-019-3045-4>
14. S. Mondal, U. Rana, S. Malik, *Chem. Commun.* **51**, 12365 (2015). <https://doi.org/10.1039/C5CC03981A>
15. M. Dinari, M.M. Momeni, M. Goudarzirad, *Surf. Eng.* **32**, 535 (2016). <https://doi.org/10.1080/02670844.2015.1108047>
16. D. Qu, M. Zheng, P. Du et al., *Nanoscale* **5**, 12272 (2013). <https://doi.org/10.1039/C3NR04402E>
17. H. Bigdeli, M. Moradi, S. Borhani, E.A. Jafari, S. Hajati, M.A. Kiani, *Physica E* **100**, 45 (2018). <https://doi.org/10.1016/j.physe.2018.03.003>
18. M.B. Tayel, M.M. Soliman, S. Ebrahim, M.E. Harb, *Synth. Met.* **217**, 237 (2016). <https://doi.org/10.1016/j.synthmet.2016.04.011>
19. M. Rahimi-Nasrabadi, V. Pourmohamadian, M.S. Karimi et al., *J. Mater. Sci. Mater. Electron.* **28**, 12391 (2017). <https://doi.org/10.1007/s10854-017-7059-3>
20. J. Zhang, J. Jiang, H. Li, X.S. Zhao, *Energy Environ. Sci.* **4**, 4009 (2011). <https://doi.org/10.1039/C1EE01354H>
21. M. Zhang, W. Liu, R. Liang, R. Tjandra, A. Yu, *Sustain Energy Fuels* **3**, 2499 (2019). <https://doi.org/10.1039/C9SE00341J>
22. D. Pan, J. Zhang, Z. Li, M. Wu, *Adv. Mater.* **22**, 734 (2010). <https://doi.org/10.1002/adma.200902825>
23. L. Li, G. Wu, G. Yang, J. Peng, J. Zhao, J.-J. Zhu, *Nanoscale* **5**, 4015 (2013). <https://doi.org/10.1039/C3NR33849E>
24. Y. Dong, J. Shao, C. Chen et al., *Carbon* **50**, 4738 (2012). <https://doi.org/10.1016/j.carbon.2012.06.002>
25. Z. Zhang, Z. Wei, M. Wan, *Macromolecules* **35**, 5937 (2002). <https://doi.org/10.1021/ma020199v>
26. X. Lu, H. Dou, S. Yang et al., *Electrochim. Acta* **56**, 9224 (2011). <https://doi.org/10.1016/j.electacta.2011.07.142>
27. M.S. Cho, S.Y. Park, J.Y. Hwang, H.J. Choi, *Mater. Sci. Eng. C* **24**, 15 (2004). <https://doi.org/10.1016/j.msec.2003.09.003>
28. F.G. de Souza, B.G. Soares, *Polym. Testing* **25**, 512 (2006). <https://doi.org/10.1016/j.polymertesting.2006.01.014>
29. T. Abdiryim, R. Jamal, I. Nurulla, *Appl. Polymer* **105**, 576 (2007). <https://doi.org/10.1002/app.26070>
30. C. Xia, X. Hai, X.-W. Chen, J.-H. Wang, *Talanta* **168**, 269 (2017). <https://doi.org/10.1016/j.talanta.2017.03.040>
31. E. Shaker Mabrouk, S. Moataz Mohamed, E.-L. Mona Mahmoud Abd, *High Perform. Polym.* **22**, 377 (2009). <https://doi.org/10.1177/0954008309103796>
32. N. Maity, A. Kuila, S. Das, D. Mandal, A. Shit, A.K. Nandi, *J. Mater. Chem. A* **3**, 20736 (2015). <https://doi.org/10.1039/C5TA06576C>
33. S. Quillard, G. Louarn, S. Lefrant, A.G. Macdiarmid, *Phys. Rev. B* **50**, 12496 (1994). <https://doi.org/10.1103/PhysRevB.50.12496>
34. X. Du, Y. Xu, L. Xiong, Y. Bai, J. Zhu, S. Mao, *Appl. Polymers.* (2014). <https://doi.org/10.1002/app.40827>
35. S. Gurunathan, J. Woong Han, E. Kim, D.-N. Kwon, J.-K. Park, J.-H. Kim, *J. Nanobiotechnol.* **12**, 41 (2014). <https://doi.org/10.1186/s12951-014-0041-9>
36. J.N. Gavvani, A. Hasani, M. Nouri, M. Mahyari, A. Salehi, *Sensors Actuators B Chem.* **229**, 239 (2016). <https://doi.org/10.1016/j.snb.2016.01.086>
37. Y. Li, Y. Zhao, H. Cheng et al., *J. Am. Chem. Soc.* **134**, 15 (2012). <https://doi.org/10.1021/ja206030c>
38. Q. Wang, Y. Wang, Q. Meng et al., *RSC Adv.* **7**, 2796 (2017). <https://doi.org/10.1039/C6RA26458A>
39. Z. Zhao, Y. Xie, *J. Power Sources* **337**, 54 (2017). <https://doi.org/10.1016/j.jpowsour.2016.10.110>
40. L. Ding, Q. Li, D. Zhou, H. Cui, H. An, J. Zhai, *J. Electroanal. Chem.* **668**, 44 (2012). <https://doi.org/10.1016/j.jelechem.2011.12.018>
41. A.K. Samantara, S. Chandra Sahu, A. Ghosh, B.K. Jena, *J. Mater. Chem. A* **3**, 16961 (2015). <https://doi.org/10.1039/C5TA03376D>
42. H. Guan, L.-Z. Fan, H. Zhang, X. Qu, *Electrochim. Acta* **56**, 964 (2010). <https://doi.org/10.1016/j.electacta.2010.09.078>
43. S.B. Kulkarni, U.M. Patil, I. Shackery et al., *J. Mater. Chem. A* **2**, 4989 (2014). <https://doi.org/10.1039/C3TA14959E>
44. J. Huang, R.B. Kaner, *Chem. Commun.* (2006). <https://doi.org/10.1039/B510956F>
45. K.S.W. Sing, *Pure Appl. Chem.* **57**, 603 (1985)
46. J. Huang, R.B. Kaner, *J. Am. Chem. Soc.* **126**, 851 (2004). <https://doi.org/10.1021/ja0371754>
47. A. Maitra, A.K. Das, R. Bera et al., *ACS Appl. Mater. Interfaces.* **9**, 5947 (2017). <https://doi.org/10.1021/acsami.6b13259>
48. Q. Cheng, K. Tao, X. Han et al., *Dalton Trans.* **48**, 4119 (2019). <https://doi.org/10.1039/c9dt00386j>
49. J. Jin, Y. Zhou, Z. Xiong et al., *Int. J. Hydrogen Energy* **43**, 8426 (2018). <https://doi.org/10.1016/j.ijhydene.2018.03.133>
50. F.S. Omar, A. Numan, N. Duraisamy, M.M. Ramly, K. Ramesh, S. Ramesh, *Electrochim. Acta* **227**, 41 (2017). <https://doi.org/10.1016/j.electacta.2017.01.006>
51. B. Sun, X. He, X. Leng et al., *RSC Adv.* **6**, 43959 (2016). <https://doi.org/10.1039/C6RA02534J>
52. G. Qiu, A. Zhu, C. Zhang, *RSC Adv.* **7**, 35330 (2017). <https://doi.org/10.1039/C7RA05235A>
53. C. Li, J. Balamurugan, N.H. Kim, J.H. Lee, *Adv. Energy Mater.* **8**, 1702014 (2018). <https://doi.org/10.1002/aenm.201702014>
54. H.B. Li, M.H. Yu, F.X. Wang et al., *Nat. Commun.* **4**, 1894 (2013). <https://doi.org/10.1038/ncomms2932>
55. M. Rahimi-Nasrabadi, H.R. Naderi, M.S. Karimi, F. Ahmadi, S.M. Pourmortazavi, *J. Mater. Sci. Mater. Electron.* **28**, 1877 (2017). <https://doi.org/10.1007/s10854-016-5739-z>
56. H.R. Naderi, A. Sobhani-Nasab, M. Rahimi-Nasrabadi, M.R. Ganjali, *Appl. Surf. Sci.* **423**, 1025 (2017). <https://doi.org/10.1016/j.apsusc.2017.06.239>
57. A. Sobhani-Nasab, H. Naderi, M. Rahimi-Nasrabadi, M.R. Ganjali, *J. Mater. Sci. Mater. Electron.* **28**, 8588 (2017). <https://doi.org/10.1007/s10854-017-6582-6>
58. A. Sobhani-Nasab, M. Rahimi-Nasrabadi, H.R. Naderi et al., *Ultrason. Sonochem.* **45**, 189 (2018). <https://doi.org/10.1016/j.ultsonch.2018.03.011>
59. H. Gao, F. Wu, X. Wang, C. Hao, C. Ge, *Int. J. Hydrogen Energy* **43**, 18349 (2018). <https://doi.org/10.1016/j.ijhydene.2018.08.018>
60. K. Adib, M. Rahimi-Nasrabadi, Z. Rezvani et al., *J. Mater. Sci. Mater. Electron.* **27**, 4541 (2016). <https://doi.org/10.1007/s10854-016-4329-4>

61. Q. Wang, H. Wang, D. Liu, P. Du, P. Liu, *Synth. Met.* **231**, 120 (2017). <https://doi.org/10.1016/j.synthmet.2017.06.018>
62. G. Oskueyan, M.M. Lakouraj, M. Mahyari, *Electrochim. Acta* **299**, 125 (2019). <https://doi.org/10.1016/j.electacta.2018.12.179>
63. M. Usman, L. Pan, M. Asif, Z. Mahmood, *J. Mater. Res.* **30**, 3192 (2015). <https://doi.org/10.1557/jmr.2015.271>
64. M.M. Sk, C.Y. Yue, K. Ghosh, R.K. Jena, *J. Power Sources* **308**, 121 (2016). <https://doi.org/10.1016/j.jpowsour.2016.01.056>
65. Y. Ma, W. Yuan, Y. Bai, H. Wu, L. Cheng, *Carbon* **154**, 292 (2019). <https://doi.org/10.1016/j.carbon.2019.07.095>
66. G. Wei, X. Zhao, K. Du et al., *Chem. Eng. J.* **326**, 58 (2017). <https://doi.org/10.1016/j.cej.2017.05.127>
67. Y. Huang, L. Lin, T. Shi et al., *Appl. Surf. Sci.* **463**, 498 (2019). <https://doi.org/10.1016/j.apsusc.2018.08.247>

Publisher's Note Springer Nature remains neutral with regard to jurisdictional claims in published maps and institutional affiliations.